© 2020. Published by The Company of Biologists Ltd | Journal of Cell Science (2020) 133, jcs243865. doi:10.1242/jcs.243865

RESEARCH ARTICLE

# Osmotic gradients induce stable dome morphogenesis on extracellular matrix

**Sumire Ishida-Ishihara[1], Masakazu Akiyama[2], Kazuya Furusawa[1,3], Isao Naguro[4], Hiroki Ryuno[4], Takamichi Sushida[5], Seiichiro Ishihara[1,6] and Hisashi Haga[1,6,*]**

## ABSTRACT

One of the fundamental processes in morphogenesis is dome formation, but many of the mechanisms involved are unexplored. Previous *in vitro* studies showed that an osmotic gradient is the driving factor of dome formation. However, these investigations were performed without extracellular matrix (ECM), which provides structural support to morphogenesis. With the use of ECM, we observed that basal hypertonic stress induced stable domes *in vitro* that have not been seen in previous studies. These domes developed as a result of ECM swelling via aquaporin water transport activity. Based on computer simulation, uneven swelling, with a positive feedback between cell stretching and enhanced water transport, was a cause of dome formation. These results indicate that osmotic gradients induce dome morphogenesis via both enhanced water transport activity and subsequent ECM swelling.

**KEY WORDS: Osmotic gradient, Epithelial cells, ECM, Swelling, Aquaporin, Numerical simulation**

## INTRODUCTION

Dome formation is one of the fundamental processes in morphogenesis. During morphogenesis, 3D shapes are formed due to bending, folding, and elongation of flat epithelial sheets (Gilmour et al., 2017). One example of bending morphogenesis is dome formation (Gilmour et al., 2017). Domes *in vivo* and *in vitro* were described in the early twentieth century (Boyd et al., 1968) and in 1969 (Leighton et al., 1969), respectively. *In vivo* dome formation is reported to occur in the early stages of villification of the mouse gut (Chin et al., 2017; Walton et al., 2016). Dome-like structures appear on flat epithelium of mouse gut and the structures grow as cell area expands. *In vitro*, domes are observed in many epithelial cell lines, such as Madin–Darby Canine Kidney (MDCK) epithelial cells, *Xenopus laevis* kidney epithelial cells and Fischer rat thyroid epithelial cells (Ichigi and Asashima, 2001; Ikuzawa et al., 2007; Latorre et al., 2018; Leighton et al., 1969, 1970; Tonoli et al., 2000). However, the driving factors of dome formation are still not fully elucidated. In dome formation during mouse gut villification, the shape of the domes formed is determined by the mesenchymal cluster beneath the epithelium, but the factor that triggers dome formation is not known. Such driving factors are suggested by the study of *in vitro* domes. *In vitro* domes are thought to form through the following steps: (1) transcellular transport of ions, which results in the interstitial increase of ion concentration at the basal side, (2) the emergence of an osmotic gradient due to the increase in ion concentration, which leads to fluid influx to the basal side, (3) generation of hydrostatic pressure by fluid-induced dome formation. Previous reports have already revealed the contribution of the transcellular transport of ions by studying the effects of treatment with an ion transport inhibitor (Ikuzawa et al., 2007; Leighton et al., 1970), and the contribution of hydrostatic pressure has been assessed using the deformation of soft polydimethylsiloxane substrates (Latorre et al., 2018). However, the role of the osmotic gradient has not been fully examined, and the reaction of epithelial sheets to osmotic gradients has not been investigated fully.

A few studies suggest that osmotic pressure and subsequent fluid regulation affects morphogenesis *in vivo*, *ex vivo* and *in vitro*. Extension of the excretory canal in *Caenorhabditis elegans in vivo* and branching morphogenesis in mouse lungs *ex vivo* are stimulated by hypertonic stress (Kolotuev et al., 2013; Nogawa and Hasegawa, 2002). Aquaporins (AQP) are a large family of water-transporting channels that regulate fluid balance in response to osmotic stress (Verkman, 2011). Overexpression of AQP8 in *C. elegans* expands the lumen of the canal, which is rescued by the broad AQP inhibitor, mercury chloride ($HgCl_2$) (Khan et al., 2013). *In vitro*, overexpressing AQP1 stimulates tubulogenesis in MDCK cells (Wang et al., 2015). These observations indicate that osmotic stress and fluid regulation by AQPs are involved in 3D shaping; however, their contribution to dome formation has not been fully examined.

Dome structures are observed both *in vivo* and *in vitro*; however, these two domes have notable differences in stability. *In vitro* domes repeatedly collapse and reform, whereas the *in vivo* domes formed during villification are maintained once their shape is established (Chin et al., 2017; Latorre et al., 2018; Leighton et al., 1969; Walton et al., 2016). The difference in stability is likely to result from differences between the scaffolds. The basal side of the *in vitro* domes is filled with fluid. Meanwhile, the basal side of *in vivo* domes is rich in extracellular matrix (ECM), which provides the structural support to 3D shape (Bonnans et al., 2014; Rozario and DeSimone, 2010). Loss of collagens, the most abundant ECM components in animal bodies, weakens the integrity of connective tissues and causes the rupture of blood vessels (Liu et al., 1997). However, previous studies have not observed the contribution of osmotic gradients to dome formation in the presence of ECM. Here, we reveal that osmotic gradients trigger dome formation in an epithelial sheet on ECM via AQP water transport and subsequent ECM swelling *in vitro*.

[1]Department of Advanced Transdisciplinary Sciences, Faculty of Advanced Life Science, Hokkaido University, N10-W8, Kita-ku, Sapporo 060-0810, Japan. [2]Meiji Institute for Advanced Study of Mathematical Sciences, Meiji University, Nakano 4-21-1, Nakano-ku, Tokyo 164-8525, Japan. [3]Faculty of Environmental and Information Sciences, Fukui University of Technology, Gakuen 3-6-1, Fukui 910-8505, Japan. [4]Graduate School of Pharmaceutical Sciences, University of Tokyo, Hongo 7-3-1, Bunkyo-ku, Tokyo 113-0033, Japan. [5]Department of Computer Science and Technology, Salesian Polytechnic, Oyamagaoka 4-6-8, Machida City, Tokyo 194-0215, Japan. [6]Soft Matter GI-CoRE, Hokkaido University, N21W11, Kita-ku, Sapporo 001-0021, Japan.

*Author for correspondence (haga@sci.hokudai.ac.jp)

M.A., 0000-0003-0233-578X; H.H., 0000-0001-9464-6723

**Handling Editor: David Glover**
**Received 10 January 2020; Accepted 11 June 2020**

Journal of Cell Science (2020) 133, jcs243865. doi:10.1242/jcs.243865

## RESULTS

### MDCK sheets form and maintain domes on ECM during basal hypertonic stress

In this study, *in vitro* experiments were performed because it is technically difficult to observe the osmotic contribution to dome formation *in vivo*. In order to confirm the osmotic contribution suggested by previous studies, we firstly investigated whether osmotic gradients induce dome formation in epithelial sheets without ECM. MDCK cells were directly seeded onto permeable membranes and exposed to an osmotic gradient (Fig. S1A). Regardless of the type of additional solutes, fluid-filled domes (F-domes) appeared after incubation with basal hypertonic stress (bHS), and not with isotonic stress (IS) (Fig. S1B–D). Consistent with previous studies (Latorre et al., 2018; Leighton et al., 1969), F-domes repeatedly collapsed and reformed (Fig. S1E, Movie 1). Once a dome is shaped, the structure is maintained *in vivo* (Chin et al., 2017; Walton et al., 2016). Therefore, the experimental system without ECM was not adequate to imitate *in vivo* dome formation.

To improve *in vitro* dome observation, we put ECM-based hydrogel (Matrigel) under the cells (Fig. 1A). However, the cell sheet was perforated on Matrigel (Fig. S1F), whereas dome formation *in vivo* begins from a nonporous monolayer. Because we previously reported that the mechanical properties of ECM affect MDCK morphologies (Imai et al., 2015; Ishida et al., 2014), we thought this pore formation could be attributed to the mechanical properties of Matrigel. Genipin (GP) is a less-cytotoxic cross-linker that modulates the mechanical properties of ECM (Sundararaghavan et al., 2008; Tsai et al., 2000). To obtain a nonporous monolayer, we modulated Matrigel with different concentrations of GP. GP crosslinking results in two unique outcomes: (1) the gel turns blue after GP crosslinking (Lee et al., 2003; Mi et al., 2000; Muzzarelli et al., 2015; Sundararaghavan et al., 2008; Takami and Suzuki, 1994), and (2) GP crosslinks absorb 590 nm light and emit strong red fluorescence (excitation/emission 510–560/590 nm, and excitation/emission 590/630 nm) (Hwang et al., 2011; Muzzarelli et al., 2015; Sundararaghavan et al., 2008). After GP treatment, the color of the Matrigel changed from pink to blue (Fig. S1G), and the absorbance at 595 nm and red fluorescence (excitation/emission 561/604 nm) increased in a GP-concentration-dependent manner (Fig. S1H,I). This absorbance shows a positive correlation with GP crosslinks (Hwang et al., 2011; Sundararaghavan et al., 2008). In previous reports, longer incubation time was found to increase the rate of GP crosslinking. However, in our methods, GP crosslinks were unchanged at 0.25 and 0.63 mM concentrations between 2 and 3 days of incubation. In our GP-treated Matrigel (GP-Matrigel) preparation, GP solution was mixed with ice-cold liquefied Matrigel at an indicated final concentration, rather than immersing the gelated Matrigel in GP solution, to initiate gelation and crosslinking. The immersion technique provides abundant GP to the gel and, hence, the longer incubation time increases the percentage of crosslinks. However, GP was limited in our protocol; thus, 0.25 and 0.63 mM GP-Matrigel might be almost completely crosslinked with 2 days of incubation. The difference in the intensity of red fluorescence between 0.63 and 1.0 mM GP-Matrigel was very small but significant. GP fluorescence is thought to be saturated at high concentrations. Atomic force microscopy (AFM) showed that GP treatment tended to increase Matrigel stiffness (Fig. S1J). These results indicate that GP crosslinked and mechanically modulated Matrigel in a concentration-dependent manner. As a result of cell seeding, the pores of the cell monolayer disappeared at a GP concentration of 0.25 mM or higher (Fig. S1F). Because GP concentration affects the 3D morphologies of MDCK cells (Imai et al., 2015), we investigated the dome formation with 0.25 mM or higher GP-Matrigel.

After overnight incubation in bHS with the improved experimental system (Fig. 1A), flat confluent MDCK sheets generated multiple round structures, which were identified as domes by 3D fluorescence observation, with 0.5, 0.63 and 0.75 mM GP-Matrigel (Fig. 1B,C; Fig. S2A,B, Movie 2). From here onward, GP was used at 0.63 mM, unless stated otherwise. The domes formed by this method were larger than the F-domes observed in Fig. S1A–E. In addition, the overexposed image of GP autofluorescence (Sundararaghavan et al., 2008) showed that the interior of these domes was filled with GP-Matrigel (Fig. 1D). Hereafter, these domes are referred to as 'gel-filled domes' (G-domes). The G-domes did not appear on porous MDCK sheets (Fig. S2C). Furthermore, the osmotic gradient was retained throughout G-dome formation (Fig. 1E). MDCK sheets with 0.25 mM GP-Matrigel in bHS formed larger G-domes than those with 0.63 mM GP-Matrigel, with the gel partially detached from the membrane, whereas no G-domes appeared with 1.0 mM GP-Matrigel (Fig. 1B; Fig. S2A). When the apical medium was hypertonic, G-domes were not visible (Fig. 1F). Even when they were incubated in bHS and the difference in osmolality was decreased, the cells remained flat (Fig. 1G). As long as bHS was high enough, neither the absolute value of the osmolality, the type of solute, nor the size of Transwell affected G-dome formation (Fig. 1H,I; Fig. S2D). Furthermore, according to time-lapse observations, G-domes did not collapse, but they persisted throughout the first 24 h with bHS (Fig. 2A; Movie 3). The structures were maintained in IS after the formation of G-domes (Fig. S2E). As G-domes were continuously exposed to bHS, they gradually grew into a large dome over the next several days (Fig. 2B–D). These results suggest that bHS induces G-domes on Matrigel at a specific GP concentration, and that GP-Matrigel provides stability to the dome structures.

### GP-Matrigel ununiformly swells during G-dome formation

To further examine the process of the formation of stable domes, we performed 3D live-cell imaging of G-dome formation with fluorescent beads to monitor deformation of the substrates. The video revealed that the gel swelled uniformly at the beginning of G-dome formation (Fig. 3A; Movie 4). Moreover, some areas stopped swelling, resulting in the appearance of G-domes. Indeed, there was a movement of the beads in the gel along the axis perpendicular to the cell sheet upon the appearance of G-domes (Fig. S3A, Movie 5). The final degree of swelling was significantly higher when using 0.63 mM GP-Matrigel in bHS than in IS (Fig. 3B). Conversely, 1.0 mM GP-Matrigel in bHS, in which no G-domes emerged, showed a significantly lower swelling rate than 0.63 mM GP-Matrigel in bHS. In addition, the 0.63 mM GP-Matrigel without cells neither swelled nor deformed into domes in bHS even though the osmotic gradient was kept (Fig. 3C,D). These results demonstrate that bHS stimulates cells to cause swelling of the GP-Matrigel during G-dome morphogenesis.

### Water transport by AQPs causes swelling of GP-Matrigel in a cell-height-dependent manner

Matrigel is a hydrogel that contains ionic groups. The swelling of hydrogels with ionic groups is greatly affected by the ionic strength of a solution (Quesada-Perez et al., 2011). AQPs are water-channel proteins in cells that respond to osmotic gradients (Deen et al., 1997; Verkman, 2011). It is possible that water transport by AQPs from apical medium to basal GP-Matrigel reduces ionic strength within

Journal of Cell Science (2020) 133, jcs243865. doi:10.1242/jcs.243865

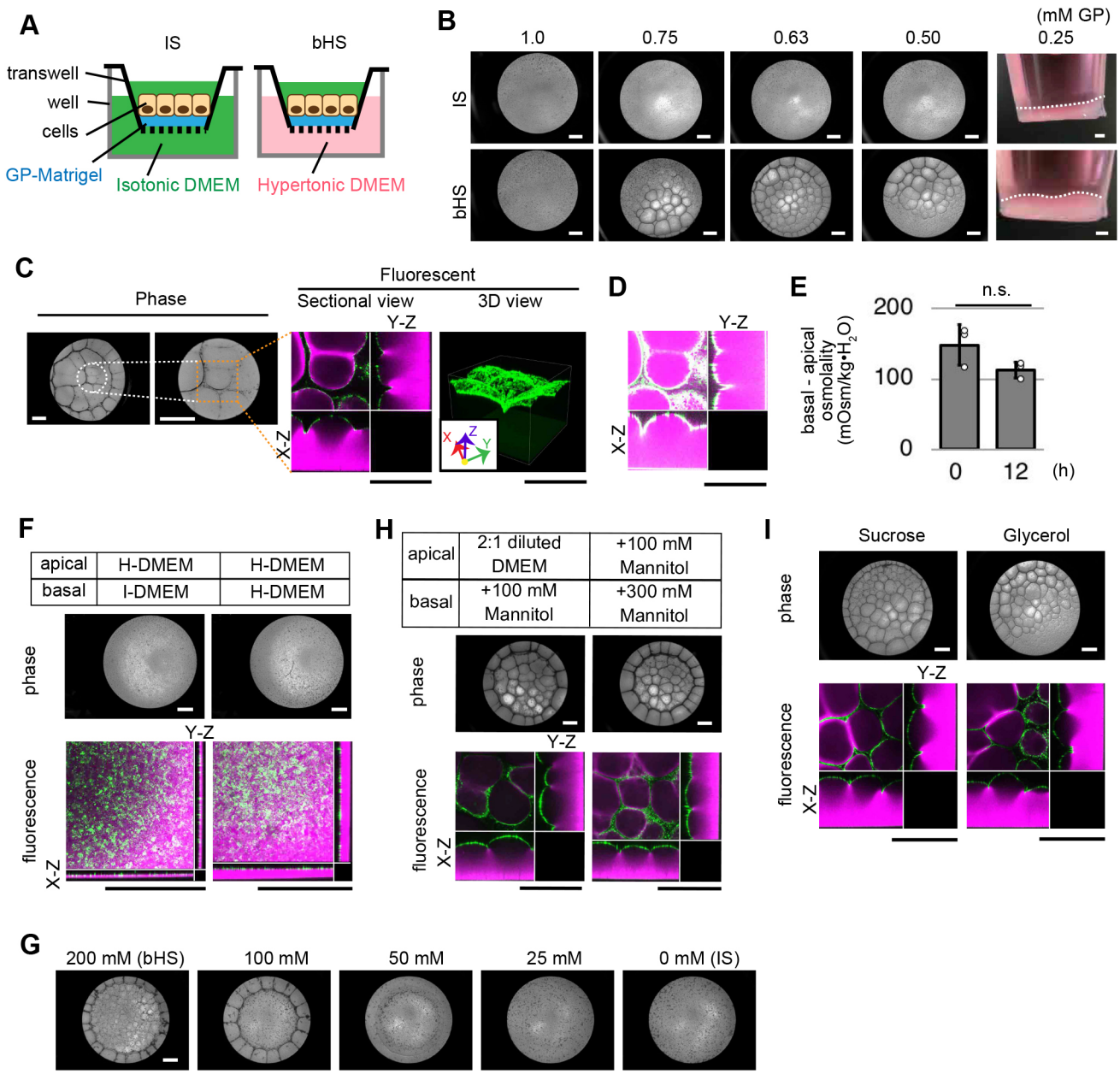


**Fig. 1. MDCK sheets formed stable domes on genipin-treated Matrigel (GP-Matrigel) at certain genipin (GP) concentrations in basal hypertonic stress.** (A) The experimental system for isotonic stress (IS) and basal hypertonic stress (bHS) treatment with GP-Matrigel. Blue, green, and pink indicate GP-Matrigel, isotonic DMEM, and hypertonic DMEM, respectively. (B) MDCK cells with fluorescent-labeled membrane (MDCK-CAAX cells) on 1.0, 0.75, 0.63 and 0.50 mM GP-Matrigel, and side views of the Transwells with the cells on 0.25 mM GP-Matrigel. White dashed lines indicate the surface of the cell sheets. (C) Phase-contrast and fluorescence images of MDCK-CAAX sheets on 0.75 mM GP-Matrigel. White and orange dashed lines indicate regions shown in the enlarged view and the fluorescence view, respectively. (D) Overexposed images of the fluorescence view shown in C. (E) Quantification of the difference in osmolality between 0 h and 12 h after bHS treatment on 0.63 mM GP-Matrigel. Data are mean±s.d. of $n$=3 independent experiments. n.s., not significant (Student's $t$-test. See details in Materials and Methods). (F) MDCK-CAAX sheets on 0.63 mM GP-Matrigel with hypertonic stress from the apical side or from both sides. (G) MDCK-CAAX sheets on 0.63 mM GP-Matrigel with bHS induced by hypertonic DMEM with different mannitol concentrations. (H) Gel-filled domes (G-domes) on 0.63 mM GP-Matrigel induced by the same osmotic difference with different osmolality. Wild-type MDCK cells were used. (I) G-domes generated by sucrose or glycerol on 0.63 mM GP-Matrigel. Scale bars: 1 mm. Images are representative of at least $n$=3 independent experiments. (C,D,F) Green, MDCK-CAAX. (H,I) Green, Calcein-AM. (C,D,F,H,I) Magenta, GP-Matrigel. These experiments used Matrigel incubated with GP for 48 h.

the gel and leads to gel swelling. To examine this hypothesis, we measured the water transport activity. When water is transported from the apical to basal side of an epithelial sheet, the Phenol Red in the apical medium becomes concentrated (Jovov et al., 1991). For 0.63 mM GP-Matrigel, the concentration of apical Phenol Red was significantly higher in bHS than in IS and did not differ with GP concentration in bHS (Fig. 4A; Fig. S3B). $HgCl_2$, a broad inhibitor of AQPs (Bai et al., 1996; Deen et al., 1997; Ishibashi et al., 1994), prevented water transport, gel swelling, and G-dome formation (Fig. 4B–D). Additionally, free water influx to GP-Matrigel by immersion in pure water without seeding cells resulted in uniform swelling and the GP-Matrigel remained flat (Fig. 4E). The surface stiffness of the gel tended to increase after swelling in water (Fig. S3C), consistent with the findings of a previous study that

Journal of Cell Science (2020) 133, jcs243865. doi:10.1242/jcs.243865

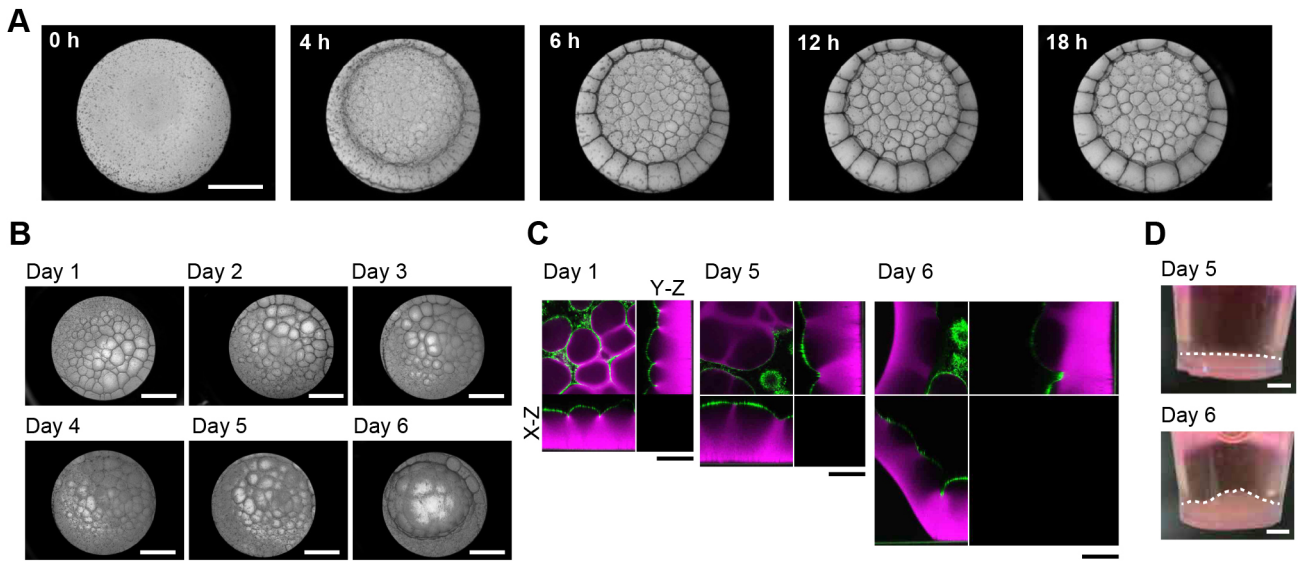


**Fig. 2. G-dome structures obtained stability.** (A) Development of G-domes over time on 0.63 mM GP-Matrigel. (B,C) Phase-contrast (B) and fluorescence (C) images of G-dome development over time on 0.63 mM GP-Matrigel in long-term culture. (D) Side views of Transwells containing G-domes on 0.63 mM GP-Matrigel. White dashed lines indicate the surfaces of the cell sheets. Images in A,B,D are representative of at least *n*=3 independent experiments. Images in C are from *n*=1 experiment (green, MDCK-CAAX: magenta, GP-Matrigel). Scale bars: 2 mm (A,B,D); 500 µm (C). These experiments used Matrigel incubated with GP for 48 h.

showed that hydrogel becomes stiffer under highly swollen conditions (Hoshino et al., 2018). These data indicate that water transport in cells by AQPs heterogeneously swells the GP-Matrigel during the formation of G-domes.

Aside from ionic strength, gel stiffness also affects the degree of swelling. The stiffness of the gel restricts the expansion of the polymer network during swelling (Quesada-Perez et al., 2011), consistent with the decrease we observed in the swelling of stiffer GP-Matrigel in pure water (Fig. S3D). Because stiffer gel had no effect on the AQP water transport (Fig. S3B), gel stiffness prevented swelling not by reducing water transport but by limiting gel expansion. These observations indicate that the absence of domes on 1.0 mM GP-Matrigel might be related to the inhibition of swelling of the stiffer gel.

To demonstrate the mechanism by which cells transport water in a dome-shaped formation, we focused on heterogeneous swelling, as shown in Fig. 3A. Cells of F-domes are stretched and become thinner than those in flat regions (Fig. S4A,B) (Latorre et al., 2018). Moreover, stretch stimuli are known to enhance AQP1 expression (Baetz et al., 2009). Before osmotic treatment, we observed that the cell height was not even (Fig. S4C). Because stretched cells became thinner (Fig. S4A,B) (Latorre et al., 2018), we hypothesized that non-uniform swelling occurs as follows: (1) thinner cells transport more water in bHS, (2) the gel locally swells due to the transported water, (3) the swollen gel stretches the cells above, (4) the stretched cells enhance water transport, and (5) the positive feedback of stages (2) to (4) leads to non-uniform gel swelling in a dome-shaped formation. To examine this, the correlation between cell thickness and water transport was investigated. Cells were seeded onto a non-coated Transwell with different cell densities and the water transport was measured in bHS. At lower cell density, the cells were thinner, whereas at higher cell density, the cells were thicker (Fig. S4D). For this experiment, we used a 1.0 µm pore membrane instead of a 0.4 µm pore. As shown in Fig. S1A–E, MDCK sheets on a 0.4 µm

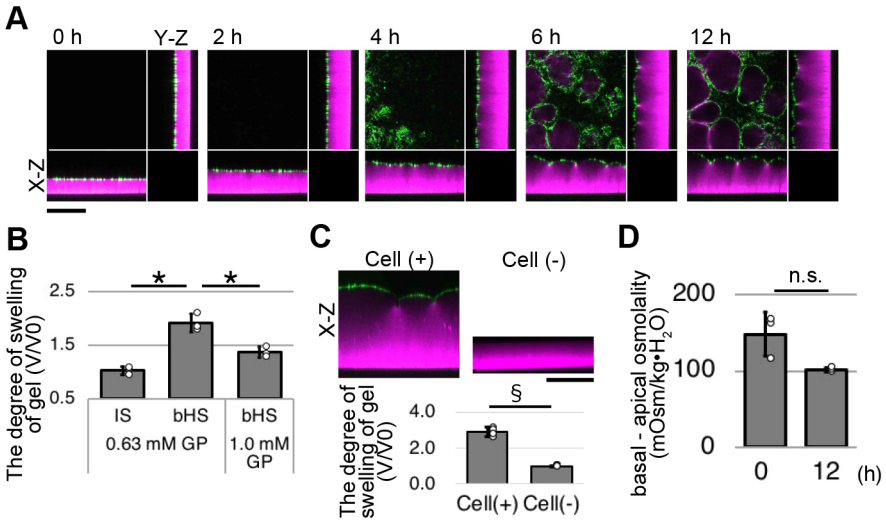


**Fig. 3. GP-Matrigel ununiformly swelled during G-dome formation.** (A) Development of G-domes over time on 0.63 mM GP-Matrigel (green, MDCK-CAAX; magenta, GP-Matrigel). (B) Gel swelling analysis of GP-Matrigel with cells. *n*=3 independent experiments. (C) Sectional views and gel swelling analysis of 0.63 mM GP-Matrigel in bHS with (+) and without (–) cells (green, MDCK-CAAX; magenta, GP-Matrigel). *n*=4 independent experiments. (D) Quantification of the difference in osmolality between 0 h and 12 h after bHS treatment without cells. 0.63 mM GP-Matrigel was used. *n*=3 independent experiments. Data are presented as mean±s.d. **P*<0.05 (Student's *t*-test with Bonferroni correction); §*P*<0.01 (Welch's *t*-test); n.s., not significant (Welch's *t*-test). Images are representative of at least *n*=3 independent experiments. Scale bars: 500 µm. Matrigel was incubated with GP for 48 h (A,B,D) or 72 h (C).

Journal of Cell Science (2020) 133, jcs243865. doi:10.1242/jcs.243865

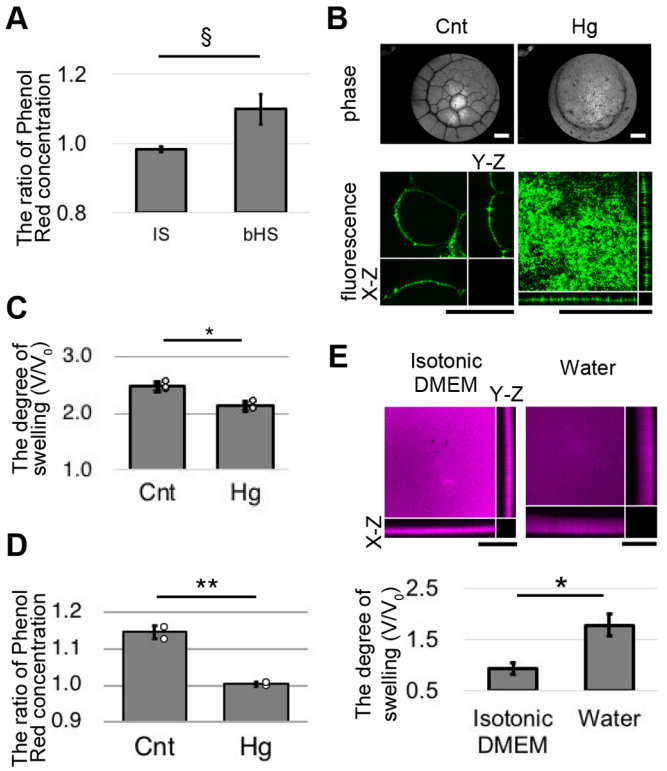


**Fig. 4. Aquaporins mediate swelling of GP-Matrigel in bHS.** (A) Water transport analysis of wild-type MDCK sheets on 0.63 mM GP-Matrigel in IS or bHS. *n*=6 independent experiments. (B,C) Images (B) and gel swelling analysis (C) of wild-type MDCK cells on 0.63 mM GP-Matrigel with $HgCl_2$ (Hg) and untreated control GP-Matrigel (Cnt). *n*=3 independent experiments. (D) Water transport analysis of wild-type MDCK sheets on 0.63 mM GP-Matrigel in bHS with (Hg) and without (Cnt) $HgCl_2$ treatment. *n*=3 independent experiments. (E) Images and gel swelling analysis of GP-Matrigel without cells after immersion in isotonic DMEM or pure water. 0.63 mM GP-Matrigel was used. *n*=6 independent experiments. (B,E) Green, calcein-AM; magenta, GP-Matrigel. Scale bars: 1 mm. Images are representative of $n \geq 3$ independent experiments. (A,C,D,E) Mean±s.d. §$P<0.05$ (Welch's *t*-test); *$P<0.01$ (Student's *t*-test); **$P<0.001$ (Student's *t*-test). These experiments used Matrigel incubated with GP for 48 h.

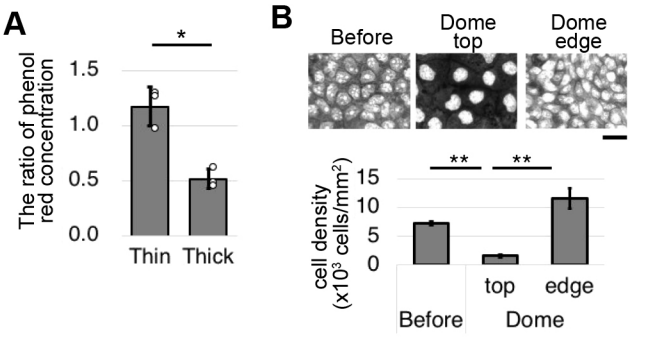


**Fig. 5. Aquaporins transported water in a cell height dependent manner.** (A) Water transport analysis of uncoated Transwells with thin or thick cells. *n*=3 independent experiments. (B) Representative images of nucleus and cell density analysis of MDCK-WT sheets on 0.63 mM GP-Matrigel. *n*=9 regions from three independent experiments. Data shown are mean±s.d. *$P<0.01$; **$P<0.0001$ with Bonferroni correction (Student's *t*-test). Scale bar: 20 µm. These experiments used Matrigel incubated with GP for 72 h (A) or 48 h (B).

pore formed F-domes in bHS, which caused cell thinning. F-domes did not appear on a 1.0 µm pore in bHS for an as yet unknown reason. To exclude the contribution of additional cell thinning, a 1.0 µm pore was used to investigate water transport with a different cell height. In this condition, water transport across cell sheets significantly increased in thinner cells (Fig. 5A). Next, we examined cell stretching in G-domes by observing the cell density because G-domes were too large to allow direct visualization of cell height under a high-power objective lens. The results exhibited that the cell density was significantly lower at the top of the G-dome than both in the preceding flat area and at the edge of the G-dome (Fig. 5B). We also tracked cell density by 3D live imaging of the cell membrane. The cell density was lower in the area of the future dome top than in the area of the future dome edge (Fig. S4E,F). Cell density at the future top decreased during G-dome formation and increased at the future edge (Fig. S4E,G). In addition, cells were fixed and inverted onto a coverslip after staining to observe their height under a high-magnification objective lens. The images of F-actin showed that the cells became thinner in the dome top than in IS (Fig. S5A–C). These findings suggest that the swollen gel stretches the cells and, as a result of this, cellular water transport is enhanced.

### Cell stretching increases the volume of the cells in MDCK monolayers

Stretch stimuli affect cellular volume and contractility. Cell spreading reduces the volume and consequently alters cellular behavior, including cell cycle progression, differentiation, and contractility (Bao et al., 2017; Guo et al., 2017; Neurohr et al., 2019). Therefore, we investigated whether stretching changes the volume of the cells in MDCK monolayers. An MDCK monolayer was isotropically stretched using a silicone rubber chamber (Takemoto et al., 2015) that resulted in an increase in cell area of 26% (±13%; mean±s.d.) (Fig. S5D). Because the nucleus also undergoes changes in response to changes in cytoplasmic volume (Guo et al., 2017), we measured the volume of the nucleus and found it to be increased (26%±14%) in stretched cells (Fig. S5D). This observation is contradictory to that previously reported. In addition, we seeded MDCK cells at different densities on glass, as described in a previous report (Guo et al., 2017), and measured the volumes of cell nuclei. The adhesion area and nuclear volume were found to be positively correlated (Pearson's correlation, 0.73) (Fig. S5E). As human mammary epithelial cells were used in the previous study, the differing results might be due to the difference in cell type.

### Actomyosin contractile force does not contribute to G-dome formation

Stretch stimuli enhances the cellular contractile force through actin filaments and myosin II (actomyosin) (Mizutani et al., 2009; Uyeda et al., 2011). We investigated the contribution of actomyosin in G-dome formation because actomyosin contractility, in general, plays a key role in morphogenesis (Diaz-de-la-Loza et al., 2018; Kasza and Zallen, 2011; Martin, 2010; Young et al., 1993). Myosin II imparts contractility through the motor activity of myosin heavy chains following phosphorylation of Ser19 and/or Thr18 of the myosin regulatory light chain (MRLC) (Mizutani et al., 2006). We performed immunofluorescence imaging for phosphorylated MRLC (P-MRLC) and inverted stained G-domes onto a coverslip to observe the shape of individual cells. As shown in Fig. S5A,B, mono-phosphorylated MRLC (1P-MRLC) and di-phosphorylated MRLC (2P-MRLC) were partially colocalized with actin filaments (F-actin) before and after G-dome formation. To investigate the contribution of actomyosin, we treated the MDCK monolayer with inhibitors of actin polymerization (cytochalasin D), myosin heavy

Journal of Cell Science (2020) 133, jcs243865. doi:10.1242/jcs.243865

chain activity (blebbistatin), and MRLC phosphorylation (Y27632) and found that cytochalasin D treatment generated perforations in the MDCK monolayer (Fig. S5F), possibly because F-actin functions to maintain epithelial integrity (Ivanov et al., 2010). Because porous monolayers did not show G-dome formation (Fig. S2C), the contribution of actomyosin was evaluated using blebbistatin and Y27632. Neither blebbistatin nor Y27632 prevented G-dome formation, although Y27632 treatment decreased the phosphorylation of MRLC (Fig. S5G–I). These results indicate that the contribution of actomyosin contractile force is negligible.

### A positive feedback between extending cells and enhanced water transport induces G-dome formation

In order to verify our conjecture that the positive feedback between an extending cell and enhanced water transport induces G-dome formation, we adopted the vertex dynamics model for representing deformations of cellular tissues. We also constructed a phenomenological 2D model introducing the interaction of the ECM interface, cells, and water that cells absorb.

In our modeling, we represented the whole structure of a cellular tissue on the gel as a set of triangular prisms; that is, a cell layer is represented by the top faces of triangular prisms (Fig. S6A,B). Our model consists of two kinds of differential equations. The first is a governing equation of vertices on a cell layer. This equation was derived as the gradient system of two potential energies of the bending energy $U^{Bend}$ and the volume conservation $U^{Volume}$. For the $i$-th vertex $\mathbb{R}_i$, it is specifically described as:

$$\tau_i \frac{d\mathbb{R}_i}{dt} = -\frac{\delta U}{\delta \mathbb{R}_i} = -\left(\frac{\delta U^{Bend}}{\delta \mathbb{R}_i} + \frac{\delta U^{Volume}}{\delta \mathbb{R}_i}\right),$$

where $\tau_i$ is a time constant. $U^{Bend}$ means that the angle between two triangular faces is preserved to a specified angle, and $U^{Volume}$ means that the volume of the whole structure, which consists of triangular prisms, is preserved to an ideal volume. Note that the ideal volume increases depending on the time that has passed since the cells started absorbing water. The second equation describes the total water that cells on the $j$-th triangle absorb. Based on our experimental observations, we assumed that the total water that cells on a triangle absorb depends on the thickness of the cells. Here we supposed that the cell thickness $c_j(t)$ on the $j$-th triangle depends on the cell area and describe the equation of the total water that cells on $j$-th triangle absorb as follows:

$$\frac{dw_j}{dt} = f(c_j),$$

note that the function $f$ is introduced based on our experimental results. In particular, it can be confirmed in numerical computations that minor changes to $f$ do not produce major differences of output patterns. Finally, we changed the time constant $\tau_i$ depending on the cell thickness. This is a mathematical assumption obtained by integrating several experimental data. See Materials and Methods for details of our model.

In our numerical computations, we evaluated our model with or without cells. Based on our experimental observations (Fig. S7), we assumed in our model that cell proliferation does not occur. As shown in Fig. 6, although the initial conditions were the same, the final states were different patterns, and some domes were formed on the circular region $\Omega$ in the case where the presence of cells was modeled. Hence, our results obtained by numerical simulations suggest that the presence of cells plays a major role in determining the final gel pattern.

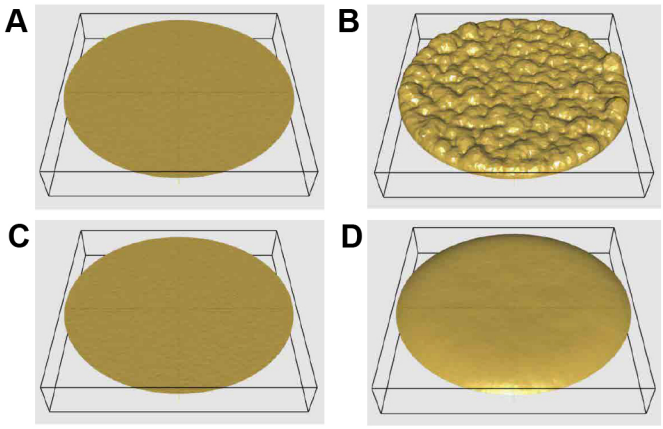


**Fig. 6. Results of numerical simulation.** (A,C) The initial state of the domes. (B,D) The final state of the domes. (B) Simulation modeling a gel with cells present, corresponding to the conditions in Fig. 3A. (D) Simulation modeling a gel without cells, corresponding to the GP-Matrigel in water condition shown in Fig. 4E. In this simulation, we set the thickness of all cells to 0.0, that is, for all index $j$, $c_j$=0.

## DISCUSSION

To the best of our knowledge, this is the first study to report that osmotic gradients induce stable dome morphogenesis. Here, we suggest a model for stable G-dome morphogenesis (Fig. 7). In response to bHS, cells started water transport in a cell height-dependent manner. Thin cells transported more water than thick cells. This led to local swelling of the GP-Matrigel and positive feedback of non-uniform water transport, resulting in G-dome formation.

The concentration of GP, which is a cross-linker that increases the viscoelasticity of biomaterials, affected G-dome appearance in bHS. We previously reported that the mechanical properties of the substrates regulate cell morphogenesis *in vitro*. Increased elasticity inhibits cyst formation by folding cell migration (Ishida et al., 2014). In addition, increased viscosity prevents formation of the tulip hat structure of a cell cluster (Imai et al., 2015). The elasticity of the gel increased in a GP concentration-dependent manner. In addition, the swelling property negatively correlated with GP concentration. Because the increase in elasticity of the gel has a negative effect on gel swelling (Quesada-Perez et al., 2011), GP crosslinking is presumed to prevent Matrigel from swelling by augmenting its elasticity.

In the presence of GP-Matrigel, the domes did not collapse but were maintained, probably owing to the difference in ground substances. F-domes are generated by the hydrostatic pressure of fluid inside the dome (Latorre et al., 2018). Ethylenediaminetetraacetic acid (EDTA) treatment generates small spaces between the cells and eliminates F-domes (Latorre et al., 2018). This minor disruption allows the immediate flow of fluid out from the domes. Conversely, G-domes were filled with GP-Matrigel, which is gelated (not in the liquid state) and may not escape from the domes following local disruption. Similarly, the mechanical plasticity of the ECM supports branching morphogenesis in the mammary gland (Buchmann et al., 2019 preprint). G-domes were maintained after removal of the osmotic gradient, indicating that the GP-Matrigel plastically deformed and supported maintenance of the dome structure.

During G-dome formation, cells at the top of the domes were stretched. Previous reports have shown smaller volumes for

Journal of Cell Science (2020) 133, jcs243865. doi:10.1242/jcs.243865

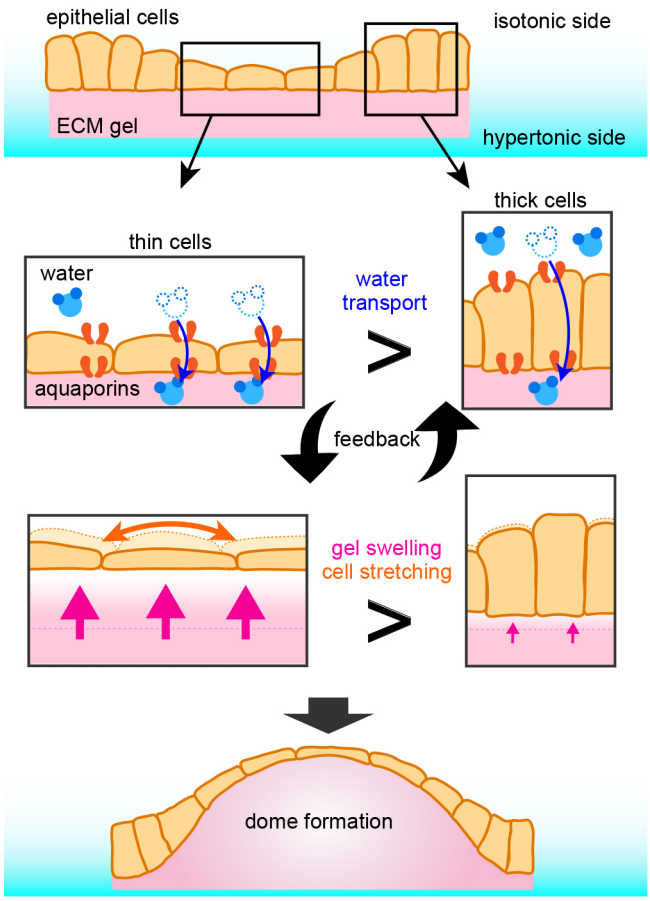


**Fig. 7. The osmotic gradient triggers G-dome formation via heterogeneous water transport and subsequent gel swelling.** In response to the osmotic gradient, MDCK cells on an ECM gel transport water via AQPs in a cell height-dependent manner. The heterogeneous water transport causes local gel swelling, which induces biased cell stretching. The stretching increases the difference in cell height, inducing a feedback loop of heterogeneous water transport. This feedback induces G-dome formation.

extended cells both in the cytoplasm and nucleus (Guo et al., 2017) and that volume changes may modify cell behavior. In our study, the nuclear volume in extended MDCK cells increased rather than decreased. The increase in the cell volume leads to a decrease in the macromolecular concentration inside the cells, inducing cell cycle arrest (Neurohr et al., 2019). We revealed that the cells at the G-dome top were stretched, and their increased volume might arrest their cycle progression. After the inhibition of cell proliferation, G-dome formation was not disrupted. Thus, the increase in the volume of stretched cells might not significantly affect the formation of G-domes.

We found that a certain degree of swelling was necessary for G-dome formation. The contribution of the ECM to morphogenesis has been actively investigated; however, the contribution of ECM swelling to morphogenesis is poorly understood. Tanaka et al. (1987) reported the appearance of a folding pattern after the swelling of the surface of hydrogels. Another group mimicked the formation of cortical convolution in the brain using gel swelling (Tallinen et al., 2016). Our findings suggest that ECM swelling might contribute to *in vivo* morphogenesis.

In conclusion, this study has found that G-dome morphogenesis is affected by the trans-epithelial osmotic gradient. The osmotic gradient triggered the swelling of GP-Matrigel, via the water transport activity of AQPs, in a cell height-dependent manner. Additionally, computer simulations demonstrated that water transport with positive feedback between cell stretching and gel swelling is important for G-dome formation. This study raises the possibility that osmotic gradients induce dome morphogenesis *in vivo* by promoting water transport by AQPs.

## MATERIALS AND METHODS

### Reagents

Dulbecco's Modified Eagle's Medium (DMEM; D6046, Sigma-Aldrich, St Louis, MO, USA) supplemented with 10% bovine fetal serum (FBS; 172912, Sigma-Aldrich) and 1% antibiotics and antimycotics (Sigma-Aldrich) was used as isotonic DMEM (I-DMEM). To prepare hypertonic DMEM (H-DMEM), mannitol (133-00845, FUJIFILM Wako Pure Chemical Corporation, Osaka, Japan) was added to I-DMEM at the concentration of 200 mM. The absolute osmolality was measured using a cryoscopic osmometer (OSMOMAT 030; Gonotec, Berlin, Germany); I-DMEM and H-DMEM were 298 (±2.5 s.d.) mOsm per kg $H_2O$ and 441.6 (±26.5 s.d.) mOsm per kg $H_2O$, respectively. Glycerol (G5516, Sigma-Aldrich) or sucrose (196-00015, FUJIFILM Wako Pure Chemical Corporation) were added to I-DMEM at the concentration of 200 mM to prepare the hypertonic DMEM of different solutes. Where the name and the concentration of solute are not mentioned, the H-DMEM was supplemented with 200 mM mannitol. We also used I-DMEM diluted with distilled water (water:I-DMEM=1:2) as hypotonic DMEM. Roscovitine was purchased from Sigma-Aldrich. 0.1 mM $HgCl_2$ (130-01151, FUJIFILM Wako Pure Chemical Corporation) was used to inhibit aquaporins. Cytochalasin D (BML-T109-0001, COSMO BIO CO., LTD, Tokyo, Japan), blebbistatin (BML-EI315-0005, COSMO BIO CO., LTD), and Y27632 (Y0503, Sigma-Aldrich) were used to inhibit actomyosin at 5, 20, and 20 µM concentrations, respectively.

### Preparation of GP-Matrigel

Matrigel (354230, Corning, NY, USA) was stored at −20°C and thawed overnight at 4°C before use. Liquified Matrigel was mixed with genipin (GP; 078-03021, FUJIFILM Wako Pure Chemical Corporation) solution on ice at final concentrations of 1.0, 0.75, 0.63, 0.50, 0.25, and 0.13 mM. 24-well and 12-well Transwell inserts with 0.4 µm pore size (353095 and 353180, CORNING) were filled with 35 µl and 105 µl of the mixture, respectively, and incubated for 48 or 72 h at 37°C for gelation and crosslinking. After the gel was rinsed with DMEM (non-serum, non-antibiotics), the gel was used for experiments. To measure the absorbance of GP crosslinking, 100 µl of GP-Matrigel mixture was added to each well of a 96-well plate (TR5003, NIPPON Genetics Co., Ltd, Tokyo, Japan). The absorbance at 595 nm wavelength was measured using a plate reader (iMark, Bio-Rad, Hercules, CA, USA). To measure the fluorescence of GP crosslinking, GP-Matrigel after 72 h incubation was observed by confocal laser-scanning microscopy (A1 confocal imaging system; Nikon Instech, Tokyo, Japan) at an excitation wavelength of 561 nm and an emission wavelength of 604 nm. The fluorescence intensity was calculated using ImageJ (National Institutes of Health, Bethesda, MD). For AFM experiments (described in below), 800 µl GP-Matrigel was prepared on a 35 mm dish.

### Atomic force microscopy

The surface stiffness of gels was measured by AFM (Nanowizard4, Bruker, Billerica, MA, USA) using a microscope (TE300, Nikon Instech). Pyramidal silicon nitride cantilevers (MLCT; Bruker) with a spring constant of 0.06 N/m, calibrated by thermal tuning using a simple harmonic oscillator model, were used. Samples were indented with a calibrated force of 0.5–1.5 nN in a scan area of 1 $\mu m^2$ (3 pixels×3 lines). The elastic properties (Young's modulus) were estimated after the application of the Hertzian model (Bilodeau, 1992) with an assumed Poisson's ratio of 0.5.

### Cell culture and osmotic stress treatment

MDCK cells were obtained from the RIKEN BRC through the National BioResource Project of the MEXT/AMED, Japan. MDCK cells were not authenticated. Mycoplasma contamination was not detected. MDCK cells

Journal of Cell Science (2020) 133, jcs243865. doi:10.1242/jcs.243865

were transfected with a phmAG1-H-Ras-CAAX vector and a stable cell line (MDCK-CAAX) was established, as previously reported (Ishida et al., 2014). The cells were cultured in I-DMEM and were incubated at 37°C in a humidified incubator with 5% $CO_2$. A trypsinized cell suspension of $2.0\times10^5$ or $4.0\times10^5$ cells was seeded onto a non-coated permeable membrane or GP-Matrigel in a 24-well Transwell insert, respectively. After cells became tightly confluent, cells were exposed to osmotic stress. After removal of the medium, 500 µl of I-DMEM and 1000 µl of H-DMEM was added to the apical and basal side of the chamber in the 24-well plate, respectively (basal hypertonic stress, bHS). As a control, 1000 µl of I-DMEM was added to the basal side of the chamber instead of H-DMEM (isotonic stress: IS). Then cells were incubated overnight at 37°C. For long-term culture with osmotic treatment, the medium of both apical and basal sides was renewed approximately every 24 h. To make subconfluent cell sheets, $1.0\times10^5$ cells were seeded onto the GP-Matrigel in 24-well Transwells. A day after seeding, cells were exposed to osmotic stress.

### Phase-contrast imaging and time-lapse observation

Phase-contrast images were taken using a phase-contrast microscope (TE300 or TE2000, Nikon Instech), equipped with a 4× or a 10× objective. WraySpect software and Q-Capture Pro software were used for still images and time-lapse observations, respectively. Wide-field images were taken using a digital camera (EX-ZR1800, CASIO COMPUTER CO. LTD., Tokyo, Japan) from an eyepiece lens of the microscope. For time-lapse observations, a culture insert was set in a handmade glass-bottom dish with 1.6 mm of inner diameter and 1.7 mm of height. Immediately after the osmotic stress was applied, the insert was sealed with mineral oil (M5904, Sigma-Aldrich) to avoid change in pH of the medium. The microscope was kept at 37°C in an acrylic resin box, and images were captured every 2.5 min or 5 min.

### Confocal observation and 3D live imaging

Non-transfected MDCK cells (MDCK-WT cells) were stained with 1 µM Calcein-AM (C396, DOJINDO LABORATORIES, Kumamoto, Japan) in I-DMEM at 37°C for 30 min. The Transwell insert was placed in a handmade glass-bottom dish and fluorescence images were obtained using a confocal microscope. For 3D live imaging, MDCK-CAAX cells were seeded on GP-Matrigel containing fluorescent beads (I-7221, Invitrogen, Carlsbad, CA, USA). Immediately after the osmotic stress was applied, the insert was sealed with mineral oil and maintained at 37°C using an STX incubator (TOKAI HIT, Shizuoka, Japan). Images were taken every 10 min.

### Fluorescent staining

Cells were fixed with 4% paraformaldehyde in phosphate-buffered saline (PBS), permeabilized with 0.5% Triton X-100 in PBS, and stained with 2 µg/ml Hoechst 33342 (14533, Sigma-Aldrich) and 1:100 diluted Alexa Fluor-647 phalloidin (A12379, Thermo Fisher Scientific, Waltham, MA, USA) in PBS overnight at 4°C. For phosphorylated MRLC staining, cells were blocked with 0.5% skim milk (Megmilk Snow Brand Co., Ltd., Tokyo, Japan) in PBS after permeabilization then incubated with primary antibodies at ∼20°C for 2 days. The primary antibodies used were anti-phospho-MRLC (Ser 19) rabbit IgG (#3671, Cell Signaling Technology, Danvers, MA, USA) and anti-phospho-MRLC (Thr18/Ser19) rabbit IgG (#3674, Cell Signaling Technology) at a dilution of 1:100. Cells were then probed with 1:500 diluted goat anti-rabbit Alexa Fluor-488 superclonal antibody (A27034, Invitrogen) and 1:100 diluted Alexa Fluor-647 phalloidin at room temperature for 2 days. Because the sample was too large to observe cells owing to the focal distance of a high magnification objective lens, it was gently removed from the insert and inverted on a coverglass. Fluorescence images were captured using confocal microscopy.

### Gel swelling analysis

The central part of a GP-Matrigel was imaged by confocal microscopy. Then the gel was exposed to osmotic stress or immersed in pure water. After incubation at 37°C, the central part of the gel was observed again, and its volume was calculated using ImageJ software.

### Water transport analysis

To analyze the transcellular water flow, we refer to a spectroscopic method developed by Jovov et al. (1991). The same number of cells ($4.0\times10^5$) were seeded onto GP-Matrigel in 24-well Transwells and cultured until becoming tightly confluent. The apical and basal compartments of the Transwell were washed with PBS. The apical compartment was then filled with 250 µl I-DMEM supplemented with additional Phenol Red (P3532, Sigma-Aldrich) at a final concentration of 224 µM. The basal compartment was filled with 500 µl of Phenol Red-free I-DMEM or Phenol Red-free H-DMEM. After incubating for 9 h at 37°C, all the apical and basal medium was collected separately into microtubes. After the weight of the medium was measured, the media were centrifuged at 15,000 rpm (14,000 ***g***) for 30 s to precipitate cell debris. The supernatant was collected in new microtubes and the absorbance at 479 nm (A479), the isosbestic point for Phenol Red, was measured using an absorption spectrometer (SmartSpec Plus; Bio-Rad). The concentration of Phenol Red was calculated according to the following formula, which was determined using a calibration curve: Phenol Red (µM)=0.0083/A479. The concentration of basal Phenol Red was corrected to apical medium using the weight of the medium and the concentration of Phenol Red. Then the corrected Phenol Red concentration of the apical medium was divided by the initial Phenol Red concentration to determine the increase in Phenol Red concentration. To analyze the correlation between cell density and water transport per cell, different numbers of cells ($1.0\times10^5$ or $4.0\times10^5$) were seeded into non-coated Transwells with 1.0 µm pore size (353104, CORNING) and cultured until confluent. Then cells were exposed to bHS and the increase in Phenol Red concentration was determined as described above. After the medium was collected, the cells were fixed and the cell density was counted, as described for the cell density assay (see below). Then, the increase in Phenol Red concentration was divided by the total number of cells on the insert.

### Cell density assay

Cells on GP-Matrigel were stained with 10 µM SYTO9 green fluorescent nucleic acid stain (S34854, Thermo Fisher Scientific) in I-DMEM, a vital stain of nuclei, for 30 min at 37°C. Cells on uncoated Transwells with 1.0 µm pore size were fixed with 4% paraformaldehyde in PBS, permeabilized with 0.5% Trion X-100 in PBS, and stained with 2 µg/ml Hoechst 33342 and 1:500 diluted Alexa Fluor 488 phalloidin (A12379, Thermo Fisher Scientific) in PBS overnight at 4°C. The cells were then observed by confocal microscopy and the nuclei were counted either using ImageJ or by hand. To track cell density, the result of 3D live imaging was used. An area with strong fluorescence was selected from different regions with varying fluorescence intensities, and cell number was manually counted. Cell density was then calculated by measuring the area change using ImageJ.

### Cell proliferation assay

MDCK-CAAX cells ($1.0\times10^5$) were seeded onto an uncoated 24-well plate. After 1 day, 10 µM roscovitine (R7772, Sigma-Aldrich) or DMSO (control) was added to the medium and incubated for 24 h at 37°C. Cells were trypsinized and suspended in 200 µl of trypsin-EDTA. 20 µl of the suspension was taken for cell counting. The suspension was mixed with 0.4% Trypan Blue solution (15250061, Thermo Fisher Scientific) at a ratio of 1:1, and the number of live cells was directly counted using a counting chamber. 2 ml of I-DMEM was added to the remaining cell suspension and centrifuged for 3 min at 1000 rpm (89 ***g***). The supernatant was aspirated and resuspended with 500 µl I-DMEM. 10 µM roscovitine or DMSO was added to the cell suspension, and all the cells were seeded on a 24-well plate. After the cells were incubated for 24 h at 37°C, cells were counted again as described above.

### Quantitative analysis of cell height

Cells on uncoated Transwells with 1.0 µm pore size were stained and observed as described for the cell density assay. A *z*-sectional area of cell sheet was calculated from a *z*-sectional view, which was randomly selected from a field of view. The area was divided by the length of the *x*-axis to calculate the average height of the cell sheet. Cells on GP-Matrigel were stained with F-actin, as described above. Cell height was measured from a

*z*-sectional view, which was randomly selected from a field of view. The tallest point of each cell was measured.

### Quantitative analysis of cell distance

Flat MDCK sheets on GP-Matrigel with IS were stained with 10 µM SYTO 9 for 30 min at 37°C and observed using confocal microscopy. Another MDCK sheet on GP-Matrigel was incubated with bHS. After the G-domes were formed, the cells were stained and observed as described above. The cell distance, defined as the distance between the centers of the nuclei, was measured using ImageJ.

### Western blot analysis

MDCK sheets on GP-Matrigel were incubated with 20 µM Y27632 in bHS overnight. Following incubation, the cells were fixed with 10% trichloroacetic acid (T9159, Sigma-Aldrich) in PBS and rinsed three times with PBS. The cells were lysed using a sample buffer (0.13 M Tris-HCl pH 6.8, 5% dithiothreitol, 2.3% sodium dodecyl sulfate, 10% glycerol, and 0.01% Bromophenol Blue), and the lysed cells were sonicated and heated at 95°C for 5 min. Cell lysates were separated on a 12.5% sodium dodecyl sulfate polyacrylamide gel and the separated protein bands were transferred onto polyvinylidene difluoride membranes (IPVH304F0, Millipore, Burlington, MA, USA). The membranes were blocked with Can Get Signal Immunoreaction Enhancer Solution 1 (NKB-101, TOYOBO, Osaka, Japan) or 0.5% skim milk in TBST (20 mM Tris-HCl, 150 mM NaCl, and 0.05% Tween 20, pH 7.5) for P-MRLCs or GAPDH, respectively. The membranes were incubated with the following primary antibodies at 4°C overnight: anti-phospho-MRLC (Ser 19/Thr 18) rabbit IgG (1:2000), anti-phospho-MRLC (Ser 19) rabbit IgG (1:1000), and anti-GAPDH mAb (1:5,000,000; AM4300, Invitrogen). After washing with TBST, the membranes were probed with 1:10,000 diluted anti-rabbit IgG HRP-linked antibody (#7074, Cell Signaling Technology) in Can Get Signal Immunoreaction Enhancer Solution 2 or 1:50,000 diluted anti-mouse IgG HRP-linked antibody (#7076, Cell Signaling Technology) in TBST solution for P-MRLCs and GAPDH, respectively, at room temperature for 1 h. The blots were developed using a ChemiDoc Touch Imaging System (Bio-Rad). Quantification of signal intensity was performed using Image Lab software (Bio-Rad).

### Nuclear volume analysis

To stretch cells, a handmade silicone rubber chamber was used, as described in our previous study (Takemoto et al., 2015). The chamber was made of a transparent silicone rubber (SH9555, Toray Dow Corning Silicone, Tokyo, Japan) and coated with 50 mg/ml fibronectin (063-05591, FUJIFILM Wako Pure Chemical Corporation) overnight at 4°C. In total, $4.0\times10^5$ cells were seeded onto the 30-mm diameter chamber and incubated for 2 days. After staining with 1 µM calcein-AM and 10 µg/ml Hoechst for 1 h at 37°C, the cells were stretched by inserting a steel ring into the ditch of the silicone chamber. Cells were observed using confocal microscopy before and after stretching. To observe cells with different densities, handmade glass-bottom dishes (16 mm diameter) were coated with 1:10 diluted Matrigel overnight at 4°C. In total, $0.2\times10^5$, $1.6\times10^5$, and $2.0\times10^5$ cells were seeded onto the dishes and incubated for 2 days. After staining with calcein-AM and Hoechst, cells were observed. Cell area and nuclear volume were measured using ImageJ. Cell area was determined from the variation in fluorescence intensity of calcein-AM.

### Mathematical model

In the subject of developmental biology, a mathematical framework called the vertex dynamics model has often been adopted for understanding the two- or three-dimensional morphogenesis of cellular tissues (Honda et al., 2004). For this reason, we constructed a vertex dynamics model, which can represent G-dome formation as induced by the presence of cells. In our vertex dynamics model, we represented a cell group on a gel in a circular region $\Omega$, which lies on a triangle, as shown in Fig. S6A. Therefore, we described the whole system as a set of $N$ triangular prisms and propose a vertex dynamics model, which consists of an equation of vertices in the triangular region representing cell groups and an equation of total water that the cells on each triangle absorb. First, we construct a governing equation of the $i$-th vertex $\mathbb{R}_i$ ($i$=1, 2, …, $M$) in the triangulated region, where the notation $M$ stands for the total number of vertices. In our modeling, we considered the following two potential energies of the bending energy and volume conservation:

$$U^{Bend} = \frac{\kappa_1}{2}\sum_{i=1}^{M}\sum_{(j,k)\in\Lambda_i}(\mathbb{N}_j\cdot\mathbb{N}_k-\cos(\theta))^2,$$

$$U^{Volume} = \frac{\kappa_2}{2}(V-V_{Ideal})^2,$$

where $\kappa_1$ and $\kappa_2$ are positive constants. The bending energy $U^{\mathrm{Bend}}$ describes an effect that an angle of two neighboring triangles with $\mathbb{R}_i$ preserves to a specified angle $\theta$. In our simulations, we specify the angle $\theta$ as $\theta=0$, that is, by employing our bending energy form, vertices move to the direction that two neighbor triangles become flat. The vectors $\mathbb{N}_j$ and $\mathbb{N}_k$ are the outward normal vectors of $j$-th triangle and $k$-th triangle, respectively, and the notation $\Lambda_i$ stands for the set of pairs ($j$, $k$) of two neighboring triangles with $\mathbb{R}_i$. In general, the formula $\kappa C^2/2$ is often adopted as the bending energy for a continuous curve, where $\kappa$ is a positive constant, and $C$ is curvature. Here, we considered a bending energy on a discrete curve, defined by a point sequence as follows. Suppose that $\theta$ is an angle between outward normal vectors for two neighboring edges on a discrete curve, and consider the energy $\kappa\theta^2/2$. If $\theta$ is sufficiently small, we have $\theta\sim C$, where the notation $a\sim b$ represents that $a$ is asymptotically equal to $b$. Hence, we obtain $\kappa C^2/2\sim O(\theta^2)$, where the notation $O$ stands for the Landau symbol. On the other hand, in our bending energy, if two vectors $\mathbb{N}_j$ and $\mathbb{N}_k$ are almost parallel, that is, the angle between $\mathbb{N}_j$ and $\mathbb{N}_k$ is sufficiently small, the following equation holds:

$$(\mathbb{N}_j\cdot\mathbb{N}_k-\cos(\theta))^2\sim(1-\cos(\theta))^2\sim O(\theta^4).$$

This implies that our bending energy formula is softer than the general formula. The formulation of $O(\theta^4)$ has been discussed previously (Kobayashi et al., 2018). In particular, it is easy to see that the energy value increases depending on the total number of triangles. However, this is intuitively strange. In the other method, the bending energy value does not change depending on the number of triangles. In order to avoid the same problem in our model, we considered the parameter $\kappa_1$ as the bending energy coefficient per unit area. Let $R$ be the radius of the circular region, and let $A$ be the average area of a triangle. We have $A\simeq\pi R^2/N$ in the initial state. Here we defined $\kappa_1=\kappa_1' A$, where $\kappa_1'$ is a positive constant. By this formulation, it might be expected that the energy value will not change even if the total number of triangles $N$ is changed. In our numerical simulation, although we fixed $\kappa_1'=100.0$ and the number of $N$ was varied from about 3000 to 12,000, similar patterns that are almost similar were obtained. However, we do not know what kind of bending energy formulation is the most appropriate when $\theta$ is large. The volume conservation energy $U^{Volume}$ describes an effect where the volume of a set of all triangular prisms preserves to an ideal value $V_{Ideal}$.

The following equation is a governing equation of the $i$-th vertex $\mathbb{R}_i$ which was obtained as the gradient system of the potential energy $U=U^{Bend}+U^{Volume}$:

$$\tau_i\frac{d\mathbb{R}_i}{dt}=-\frac{\delta U}{\delta\mathbb{R}_i},$$

where the term $\delta U/\delta\mathbb{R}_i$ stands for the functional derivative of $U$ and the time constant $\tau_i$ is explained in the later part of this section.

Second, the equation of the total water that cells on $j$-th triangle absorb is described as follows:

$$\frac{dw_j}{dt}=f(c_j),$$

where the function $f(c_j)=(\tanh(\mu(c_0-c))+1)/2$ was specified from our experimental observations. The variable $c_j$ stands for cells thickness on the $j$-th triangle, where $c_0$ and $\mu$ are positive constants. Note that in our model, the thickness $c_j$ is calculated as the height at the centroid of the $j$-th triangle (see Fig. S6B). Since we have $\lim_{c\to0}f(c)=1$ and $\lim_{c\to\infty}f(c)=0$, when the

thickness of the cells are small the absorption of water is large, and vice versa. The function type of $f(c_j)$ was introduced based on our experimental results. We do not fully understand the relationship between the height of the cells and the amount of water absorbed. However, as shown in Fig. 5A, thin cells absorb more water than when they are taller. From this fact, we adopted the function $f$ as the simplest nonlinear function. As can be seen from the above equation, when $c$ is greater than $c_0$, the cell hardly absorbs water, and vice versa. Therefore, the parameter $c_0$ must be determined appropriately. Therefore, we defined $c_0$ as the mean height of cells. The initial height of cells was set as a uniform random number in the closed interval [0.8, 1.2], as described below. Therefore, in this case, it was reasonable to set $c_0$ to approximately 1.0. Note that if you change the initial cells' height, $c_0$ will change as well. In this sense, the setting of parameter $c_0$ is not so strict. The parameter $\mu$ is an important one that changes the shape of the function $f$. In particular, it can be confirmed in numerical computations that minor changes do not produce major differences of output patterns. In addition, when cells absorb water, the volume of the whole structure (the set of triangular prisms) increases. That is, the ideal value $V_{Ideal}$ at the time $t$ is described by:

$$V_{Ideal}(t) = V_{Init} + \rho \sum_{j=1}^{N} w_j(t)\, A_j(t),$$

where the notation $V_{Init}$ stands for the initial volume for the whole of triangular prisms, and the notation $A_j(t)$ stands for the area of $j$-th triangle at the time $t \geq 0$. $\rho$ is a positive constant. In our model, the amount of water absorbed was not scaled. Therefore, it was necessary to convert the amount of absorbed water to the ideal volume using the parameter $\rho$. We supposed that the thickness of the cell $c_j$ depends on the cell area, and we define the thickness $c_j(t)$ at the time $t > 0$ by:

$$c_j(t) = c_j(0)\left(\frac{A_j(0)}{A_j(t)}\right).$$

As you can see from the equation, the volume of the cells on each triangular prism is constant.

In our model, from our observations (Fig. S7), we assumed that cell proliferation does not occur. Moreover, we confirmed that the displacement of the gel is small when the thickness of the cell is large. Therefore, we assumed that the time constant of vertices of the $j$-th triangle is large when $c_j$ is large, and that it is small when $c_j$ is small. Note that this is the most important assumption in our mathematical model. In our vertex dynamics model, since some triangles share the $i$-th vertex $\mathbb{R}_i$, we define the time constant $\tau_i$ of $\mathbb{R}_i$ as follows:

$$\tau_i = \frac{1}{\Pi_i} \sum_{j \in \Pi_i} \frac{1}{f(c_j)}.$$

In the above definition, the notation $\#\Pi_i$ stands for the number of elements contained in the set $\Pi_i$ which contains the labels' $j$-th triangles, along with the vertex $\mathbb{R}_i$. If we removed this assumption, we could not obtain dome-like patterns.

### Initial state, boundary condition, and terminated condition

First, we determined the initial state of our numerical simulation. Let $\Omega$ be a circular region given as a disk with the specified radius $R$=12 and consider a triangulation on the region $\Omega$, which was produced using Wolfram Mathematica. As the boundary condition, vertices on the boundary of $\Omega$ were fixed ($z$=1), and the other vertices were given small perturbations (see Fig. 7A,C). The thickness $c_j$ defined at the $j$-th triangle was given a uniform random number in the closed interval [0.8,1.2]. Also, the initial value of the variable $w_j(t)$ for all indices $j$ was given as $w_j(0)$=0. In the process of determination of the initial state, we used the Mersenne Twister method (Matsumoto and Nishimura, 1998) for pseudorandom number generation. Moreover, we adopted values of parameters as listed in Table S1. Second, in some numerical simulations, since self-intersection of two triangles occurs, we used a mathematical condition for self-intersection, and if its condition was satisfied, we then terminated the numerical simulation.

### Computational method and visualization

We solved our vertex dynamics model by using a variation of the embedded Runge–Kutta method – the Bogacki–Shampine method (Bogacki and Shampine, 1996), adapting the absolute and relative tolerance values. We confirmed that if the absolute and relative tolerance values were smaller than ones listed in Table S1, the final pattern did not change. Our numerical results were visualized by our graphical library named Graphics Library for Scientific Computing (G.L.S.C.) 3D, developed by M. A., Kazuma Tateiri (Hokkaido University, Japan), T.S., and Ryo Kobayashi (Hiroshima University, Japan).

The simulation was newly programmed using the C++ language. As mentioned above, we used the embedded Runge–Kutta method for time evolution and G.L.S.C. 3D for visualization. These methods are available as a calculation library on the author's (M.A.) homepage (see http://www.isc.meiji.ac.jp/~akiyama_masakazu/).

### Quantification and statistical analysis

Each experimental condition is described in the figure legends. The error bars represent the mean±s.d. For small sample sizes ($n$<5), individual data points were also plotted. For comparison between the two values, both data sets were checked to determine whether they meet the normal distribution using the Kolmogorov–Smirnov test, in which $P$>0.05 indicates the normal distribution. Then the variance of the two data sets was verified whether significantly different or not by using an $F$-test, in which $P$<0.05 indicates the variance was significantly different. For data sets without statistically different variances, a two-sided Student's $t$-test was used to analyze the significance. For data sets with statistically different variances, a two-sided Welch's $t$-test was used to determine the statistical significance. In Student's $t$-test and Welch's $t$-test, $P$<0.05 indicates statistical significance. For comparison between values without variance, the data were tested by 99% confidence interval. The significance estimated by Student's $t$-test, Welch's $t$-test, and confidence interval is indicated with *, §, and †, respectively. For multiple comparisons, Bonferroni correction was used. Cells that were not healthy during data acquisition were excluded from the analysis.

#### Acknowledgements

We thank H. Sekihara for the technical support. We thank Professor H. Koyama and Y. Kobayashi for discussing mathematical models.

#### Competing interests

The authors declare no competing or financial interests.

#### Author contributions

Conceptualization: S. Ishida-Ishihara, M.A., K.F., S. Ishihara, H.H.; Methodology: S. Ishida-Ishihara, M.A., K.F., I.N., T.S., S. Ishihara, H.H.; Software: M.A., T.S.; Validation: S. Ishida-Ishihara; Formal analysis: S. Ishida-Ishihara, M.A., T.S.; Investigation: S. Ishida-Ishihara, H.R., S. Ishihara; Resources: S. Ishida-Ishihara, M.A., T.S.; Writing - original draft: S. Ishida-Ishihara, M.A., T.S., S. Ishihara; Writing - review & editing: S. Ishida-Ishihara, S. Ishihara; Visualization: S. Ishida-Ishihara, M.A.; Supervision: H.H.; Project administration: S. Ishida-Ishihara, M.A., H.H.; Funding acquisition: S. Ishida-Ishihara, M.A., H.H.

#### Funding

S.I.-I. was supported by a Japan Society for the Promotion of Science Research Fellowship for Young Scientists (grant number 17J06276). This work was supported by Japan Society for the Promotion of Science KAKENHI grant numbers 15H05856, 15H05857, 15H05858, 15K21726 and Global Station for Soft Matter, a project of the Global Institution for Collaborative Research and Education, Hokkaido University.

#### Supplementary information

Supplementary information available online at
https://jcs.biologists.org/lookup/doi/10.1242/jcs.243865.supplemental

#### References

**Baetz, N. W., Hoffman, E. A., Yool, A. J. and Stamer, W. D.** (2009). Role of aquaporin-1 in trabecular meshwork cell homeostasis during mechanical strain. *Exp. Eye Res.* **89**, 95-100. doi:10.1016/j.exer.2009.02.018

**Bai, L., Fushimi, K., Sasaki, S. and Marumo, F.** (1996). Structure of aquaporin-2 vasopressin water channel. *J. Biol. Chem.* **271**, 5171-5176. doi:10.1074/jbc.271.9.5171

**Bao, M., Xie, J., Piruska, A. and Huck, W. T. S.** (2017). 3D microniches reveal the importance of cell size and shape. *Nat. Commun.* **8**, 1962. doi:10.1038/s41467-017-02163-2
**Bilodeau, G. G.** (1992). Regular pyramid punch problems . *J. Appl. Mech.* **59**, 512-523.
**Bogacki, P. and Shampine, L. F.** (1996). An efficient Runge-Kutta (4,5) pair. *Comput. Math. Appl.* **32**, 15-28. doi:10.1016/0898-1221(96)00141-1
**Bonnans, C., Chou, J. and Werb, Z.** (2014). Remodelling the extracellular matrix in development and disease. *Nat. Rev. Mol. Cell Biol.* **15**, 786-801. doi:10.1038/nrm3904
**Boyd, J. D., Hamilton, W. J. and Boyd, C. A.** (1968). The surface of the syncytium of the human chorionic villus. *J. Anat.* **102**, 553-563.
**Buchmann, B., Meixner, L. K., Fernandez, P., Huttere, F. P., Raich, M. K., Scheel, C. H. and Bausch, A. R.** (2019). Mechanical plasticity of the ECM directs invasive branching morphogenesis in human mammary gland organoids. *bioRxiv*.
**Chin, A. M., Hill, D. R., Aurora, M. and Spence, J. R.** (2017). Morphogenesis and maturation of the embryonic and postnatal intestine. *Semin. Cell Dev. Biol.* **66**, 81-93. doi:10.1016/j.semcdb.2017.01.011
**Deen, P. M. T., Nielsen, S., Bindels, R. J. M. and van Os, C. H.** (1997). Apical and basolateral expression of aquaporin-1 in transfected MDCK and LLC-PK cells and functional evaluation of their transcellular osmotic water permeabilities. *Pflugers Arch.* **433**, 780-787. doi:10.1007/s004240050345
**Diaz-de-la-Loza, M.-D., Ray, R. P., Ganguly, P. S., Alt, S., Davis, J. R., Hoppe, A., Tapon, N., Salbreux, G. and Thompson, B. J.** (2018). Apical and basal matrix remodeling control epithelial morphogenesis. *Dev. Cell* **46**, 23-39.e5. doi:10.1016/j.devcel.2018.06.006
**Gilmour, D., Rembold, M. and Leptin, M.** (2017). From morphogen to morphogenesis and back. *Nature* **541**, 311-320. doi:10.1038/nature21348
**Guo, M., Pegoraro, A. F., Mao, A., Zhou, E. H., Arany, P. R., Han, Y., Burnette, D. T., Jensen, M. H., Kasza, K. E., Moore, J. R. et al.** (2017). Cell volume change through water efflux impacts cell stiffness and stem cell fate. *Proc. Natl. Acad. Sci. USA* **114**, E8618-E8627. doi:10.1073/pnas.1705179114
**Honda, H., Tanemura, M. and Nagai, T.** (2004). A three-dimensional vertex dynamics cell model of space-filling polyhedra simulating cell behavior in a cell aggregate. *J. Theor. Biol.* **226**, 439-453. doi:10.1016/j.jtbi.2003.10.001
**Hoshino, K.-I., Nakajima, T., Matsuda, T., Sakai, T. and Gong, J. P.** (2018). Network elasticity of a model hydrogel as a function of swelling ratio: from shrinking to extreme swelling states. *Soft Mat.* **14**, 9693-9701. doi:10.1039/C8SM01854E
**Hwang, Y.-J., Larsen, J., Krasieva, T. B. and Lyubovitsky, J. G.** (2011). Effect of genipin crosslinking on the optical spectral properties and structures of collagen hydrogels. *ACS Appl. Mater. Interfaces* **3**, 2579-2584. doi:10.1021/am200416h
**Ichigi, J. and Asashima, M.** (2001). Dome formation and tubule morphogenesis by Xenopus kidney A6 cell cultures exposed to microgravity simulated with a 3D-clinostat and to hypergravity. *In Vitro Cell. Dev. Biol. Anim.* **37**, 31-44. doi:10.1290/1071-2690(2001)037<0031:DFATMB>2.0.CO;2
**Ikuzawa, M., Akiduki, S. and Asashima, M.** (2007). Gene expression profile of X*enopus* A6 cells cultured under random positioning machine shows downregulation of ion transporter genes and inhibition of dome formation. *Adv. Space Res.* **40**, 1694-1702. doi:10.1016/j.asr.2007.08.014
**Imai, M., Furusawa, K., Mizutani, T., Kawabata, K. and Haga, H.** (2015). Three-dimensional morphogenesis of MDCK cells induced by cellular contractile forces on a viscous substrate. *Sci. Rep.* **5**, 14208. doi:10.1038/srep14208
**Ishibashi, K., Sasaki, S., Fushimi, K., Uchida, S., Kuwahara, M., Saito, H., Furukawa, T., Nakajima, K., Yamaguchi, Y. and Gojobori, T.** (1994). Molecular cloning and expression of a member of the aquaporin family with permeability to glycerol and urea in addition to water expressed at the basolateral membrane of kidney collecting duct cells. *Proc. Natl. Acad. Sci. USA* **91**, 6269-6273. doi:10.1073/pnas.91.14.6269
**Ishida, S., Tanaka, R., Yamaguchi, N., Ogata, G., Mizutani, T., Kawabata, K. and Haga, H.** (2014). Epithelial sheet folding induces lumen formation by Madin-Darby canine kidney cells in a collagen gel. *PLoS ONE* **9**, e99655. doi:10.1371/journal.pone.0099655
**Ivanov, A. I., Parkos, C. A. and Nusrat, A.** (2010). Cytoskeletal regulation of epithelial barrier function during inflammation. *Am. J. Pathol.* **177**, 512-524. doi:10.2353/ajpath.2010.100168
**Jovov, B., Wills, N. K. and Lewis, S. A.** (1991). A spectroscopic method for assessing confluence of epithelial cell cultures. *Am. J. Physiol.* **261**, C1196-C1203. doi:10.1152/ajpcell.1991.261.6.C1196
**Kasza, K. E. and Zallen, J. A.** (2011). Dynamics and regulation of contractile actin-myosin networks in morphogenesis. *Curr. Opin. Cell Biol.* **23**, 30-38. doi:10.1016/j.ceb.2010.10.014
**Khan, L. A., Zhang, H., Abraham, N., Sun, L., Fleming, J. T., Buechner, M., Hall, D. H. and Gobel, V.** (2013). Intracellular lumen extension requires ERM-1-dependent apical membrane expansion and AQP-8-mediated flux. *Nat. Cell Biol.* **15**, 143-156. doi:10.1038/ncb2656
**Kobayashi, Y., Yasugahira, Y., Kitahata, H., Watanabe, M., Natsuga, K. and Nagayama, M.** (2018). Interplay between epidermal stem cell dynamics and dermal deformation. *NPJ Comput. Mater.* **4**, 45. doi:10.1038/s41524-018-0101-z
**Kolotuev, I., Hyenne, V., Schwab, Y., Rodriguez, D. and Labouesse, M.** (2013). A pathway for unicellular tube extension depending on the lymphatic vessel determinant Prox1 and on osmoregulation. *Nat. Cell Biol.* **15**, 157-168. doi:10.1038/ncb2662
**Latorre, E., Kale, S., Casares, L., Gómez-González, M., Uroz, M., Valon, L., Nair, R. V., Garreta, E., Montserrat, N., Del Campo, A. et al.** (2018). Active superelasticity in three-dimensional epithelia of controlled shape. *Nature* **563**, 203-208. doi:10.1038/s41586-018-0671-4
**Lee, S.-W., Lim, J.-M., Bhoo, S.-H., Paik, Y.-S. and Hahn, T.-R.** (2003). Colorimetric determination of amino acids using gene-in from Gardenia jasminoides. *Anal. Chim. Acta* **480**, 267-274. doi:10.1016/S0003-2670(03)00023-0
**Leighton, J., Brada, Z., Estes, L. W. and Justh, G.** (1969). Secretory activity and oncogenicity of a cell line (MDCK) derived from canine kidney. *Science* **163**, 472-473. doi:10.1126/science.163.3866.472
**Leighton, J., Estes, L. W., Mansukhani, S. and Brada, Z.** (1970). A cell line derived from normal dog kidney (MDCK) exhibiting qualities of papillary adenocarcinoma and of renal tubular epithelium. *Cancer* **26**, 1022-1028. doi:10.1002/1097-0142(197011)26:5<1022::AID-CNCR2820260509>3.0.CO;2-M
**Liu, X., Wu, H., Byrne, M., Krane, S. and Jaenisch, R.** (1997). Type III collagen is crucial for collagen I fibrillogenesis and for normal cardiovascular development. *Proc. Natl. Acad. Sci. USA* **94**, 1852-1856. doi:10.1073/pnas.94.5.1852
**Martin, A. C.** (2010). Pulsation and stabilization: contractile forces that underlie morphogenesis. *Dev. Biol.* **341**, 114-125. doi:10.1016/j.ydbio.2009.10.031
**Matsumoto, M. and Nishimura, T.** (1998). Mersenne twister: A 623-dimensionally equidistributed uniform pseudo-random number generator. *ACM Trans. Model. Comput. Simul.* **8**, 27. doi:10.1145/272991.272995
**Mi, F.-L., Sung, H.-W. and Shy, S.-S.** (2000). Synthesis and characterization of a novel chitosan-based network prepared using naturally occurring crosslinker. *Phlymer Chem.* **38**, 2804-2814. doi:10.1002/1099-0518(20000801)38:15<2804::AID-POLA210>3.0.CO;2-Y
**Mizutani, T., Haga, H., Koyama, Y., Takahashi, M. and Kawabata, K.** (2006). Diphosphorylation of the myosin regulatory light chain enhances the tension acting on stress fibers in fibroblasts. *J. Cell. Physiol.* **209**, 726-731. doi:10.1002/jcp.20773
**Mizutani, T., Kawabata, K., Koyama, Y., Takahashi, M. and Haga, H.** (2009). Regulation of cellular contractile force in response to mechanical stretch by diphosphorylation of myosin regulatory light chain via RhoA signaling cascade. *Cell Motil. Cytoskeleton* **66**, 389-397. doi:10.1002/cm.20378
**Muzzarelli, R. A., El Mehtedi, M., Bottegoni, C., Aquili, A. and Gigante, A.** (2015). Genipin-crosslinked chitosan gels and scaffolds for tissue engineering and regeneration of cartilage and bone. *Mar. Drugs* **13**, 7314-7338. doi:10.3390/md13127068
**Neurohr, G. E., Terry, R. L., Lengefeld, J., Bonney, M., Brittingham, G. P., Moretto, F., Miettinen, T. P., Vaites, L. P., Soares, L. M., Paulo, J. A. et al.** (2019). Excessive cell growth causes cytoplasm dilution and contributes to senescence. *Cell* **176**, 1083-1097.e18. doi:10.1016/j.cell.2019.01.018
**Nogawa, H. and Hasegawa, Y.** (2002). Sucrose stimulates branching morphogenesis of embryonic mouse lung in vitro: a problem of osmotic balance between lumen fluid and culture medium. *Dev. Growth Differ.* **44**, 383-390. doi:10.1046/j.1440-169X.2002.00651.x
**Quesada-Perez, M., Maroto-Centeno, J. A., Forcada, J. and Hidalgo-Alvarez, R.** (2011). Gel swelling theories: the classical formalism and recent approaches. *Soft Mat.* **7**, 10536-10547. doi:10.1039/c1sm06031g
**Rozario, T. and DeSimone, D. W.** (2010). The extracellular matrix in development and morphogenesis: a dynamic view. *Dev. Biol.* **341**, 126-140. doi:10.1016/j.ydbio.2009.10.026
**Sundararaghavan, H. G., Monteiro, G. A., Lapin, N. A., Chabal, Y. J., Miksan, J. R. and Shreiber, D. I.** (2008). Genipin-induced changes in collagen gels: correlation of mechanical properties to fluorescence. *J. Biomed. Mater. Res. A* **87A**, 308-320. doi:10.1002/jbm.a.31715
**Takami, M. and Suzuki, Y.** (1994). Hydrophobic blue pigment formation from phosphatidylgenipin. *J. Nutr. Sci. Vitaminol.* **40**, 505-509. doi:10.3177/jnsv.40.505
**Takemoto, K., Ishihara, S., Mizutani, T., Kawabata, K. and Haga, H.** (2015). Compressive stress induces dephosphorylation of the myosin regulatory light chain via RhoA phosphorylation by the adenylyl cyclase/protein kinase A signaling pathway. *PLoS ONE* **10**, e0117937. doi:10.1371/journal.pone.0117937
**Tallinen, T., Chung, J. Y., Rousseau, F., Girard, N., Lefèvre, J. and Mahadevan, L.** (2016). On the growth and form of cortical convolutions. *Nat. Phys.* **12**, 588-593. doi:10.1038/nphys3632
**Tanaka, T., Sun, S.-T., Hirokawa, Y., Katayama, S., Kucera, J., Hirose, Y. and Amiya, T.** (1987). Mechanical instability of gels at the phase transition. *Nature* **325**, 796-798. doi:10.1038/325796a0
**Tonoli, H., Flachon, V., Audebet, C., Callé, A., Jarry-Guichard, T., Statuto, M., Rousset, B. and Munari-Silem, Y.** (2000). Formation of three-dimensional thyroid follicle-like structures by polarized FRT cells made communication competent by transfection and stable expression of the connexin-32 gene. *Endocrinology* **141**, 1403-1413. doi:10.1210/endo.141.4.7400

**Tsai, C.-C., Huang, R.-N., Sung, H.-W. and Liang, H. C.** (2000). In vitro evaluation of the genotoxicity of a naturally occurring crosslinking agent (genipin) for biologic tissue fixation. *J. Biomed. Mater. Res.* **52**, 58-65. doi:10.1002/1097-4636(200010)52:1<58::AID-JBM8>3.0.CO;2-0

**Uyeda, T. Q. P., Iwadate, Y., Umeki, N., Nagasaki, A. and Yumura, S.** (2011). Stretching actin filaments within cells enhances their affinity for the myosin II motor domain. *PLoS ONE* **6**, e26200. doi:10.1371/journal.pone.0026200

**Verkman, A. S.** (2011). Aquaporins at a glance. *J. Cell Sci.* **124**, 2107-2112. doi:10.1242/jcs.079467

**Walton, K. D., Freddo, A. M., Wang, S. and Gumucio, D. L.** (2016). Generation of intestinal surface: an absorbing tale. *Development* **143**, 2261-2272. doi:10.1242/dev.135400

**Wang, W., Li, F., Sun, Y., Lei, L., Zhou, H., Lei, T., Xia, Y., Verkman, A. S. and Yang, B.** (2015). Aquaporin-1 retards renal cyst development in polycystic kidney disease by inhibition of Wnt signaling. *FASEB J.* **29**, 1551-1563. doi:10.1096/fj.14-260828

**Young, P. E., Richman, A. M., Ketchum, A. S. and Kiehart, D. P.** (1993). Morphogenesis in Drosophila requires nonmuscle myosin heavy chain function. *Genes Dev.* **7**, 29-41. doi:10.1101/gad.7.1.29